Check for updates

Advanced Materials

ADVANCED MATERIALS
www.advmat.de

RESEARCH ARTICLE OPEN ACCESS

Chiral Phonon–Driven Ultrafast Spin Currents in a Non-Magnetic Ferroelectric

Thomas B. Gill[1] | Ahmet Yagmur[2] | Matthew Rogers[2] | Luke Benson[2] | Nathan Fox[1] | Ben Muggleton[1,3] | Zabeada Aslam[4] | Conor McCluskey[5] | Phoenix Robinson[1,3] | Oscar Cespedes[2] | Bryan Hickey[2] | Timothy Moorsom[2,3] | Marty Gregg[5] | Edmund H. Linfield[1] | Sukhdeep Dhillon[6] | Satoshi Sasaki[2] | Joshua R. Freeman[1]

[1]School of Electronic and Electrical Engineering, University of Leeds, Leeds, UK | [2]School of Physics & Astronomy, University of Leeds, Leeds, UK | [3]School of Chemical and Process Engineering, University of Leeds, Leeds, UK | [4]LEMAS, Bragg Centre for Materials Research, University of Leeds, Leeds, UK | [5]Centre for Quantum Materials and Technologies, School of Maths and Physics, Queen's University Belfast, Belfast, UK | [6]Laboratoire de Physique de l'Ecole Normale Supérieur, ENS, Université PSL, CNRS, Sorbonne Université, Paris, France

Correspondence: Thomas B. Gill (t.b.gill@leeds.ac.uk) | Joshua R. Freeman (j.r.freeman@leeds.ac.uk)

Received: 15 April 2026 | **Revised:** 5 October 2026 | **Accepted:** 7 October 2026

Keywords: chiral phonons | spintronics | terahertz generation | ultrafast spin currents

ABSTRACT

The discovery that fundamental lattice vibrations can carry angular momentum allows non-magnetic materials to exhibit properties that until now have only been observable in magnetic materials. However, the role of these specific vibrations, commonly known as chiral phonons, in driving ultrafast spin dynamics has not yet been explored experimentally. Here, using broadband terahertz emission spectroscopy, we demonstrate that the non-magnetic ferroelectric In_2Se_3 generates signals consistent with a ultrafast spin current after excitation with an ultrafast laser pulse, which we attribute to a chiral phonon–induced spin Seebeck effect. We suggest that the transient heating creates an non-equilibrium phonon distribution, resulting in a net angular momentum and magnetization perpendicular to the thermal gradient, which is converted into a terahertz electromagnetic pulse via an inverse spin-Hall effect in a thin metal overlayer. The emitted field reverses sign upon flipping the sample orientation or replacing Pt with W, consistent with spin-current generation. Polarization-resolved measurements reveal controllable terahertz ellipticity, indicating an additional polarization-dependent ultrafast response. Our results establish chiral phonons as a route for generating ultrafast spin currents in non-magnetic materials as well as providing a pathway toward terahertz sources with switchable handedness.

1 | Introduction

Phonons are the quantized vibrations of atoms within a solid crystal lattice and have been studied for almost a century. Much more recently, it has been discovered that when these atoms perform circular motion around their equilibrium positions, they can exhibit definite chirality (parity asymmetry) [1, 2] and carry angular momentum [3]. Since this discovery, there have been reports of chiral phonons, and more generally, *axial phonons*, in a range of materials from cuprate superconductors [4], to perovskites [5], polar antiferromagnets [6], and transition metal dichalcogenides [7]. The crucial finding that phonons can carry angular momentum raises the prospect of using phonons to induce magnetic properties in non-magnetic materials, with far-reaching implications from fundamental understanding of magnetism to applications in information storage and transfer [8].

This is an open access article under the terms of the Creative Commons Attribution License, which permits use, distribution and reproduction in any medium, provided the original work is properly cited.
© 2026 The Author(s). *Advanced Materials* published by Wiley-VCH GmbH

This realization has led to a flurry of activity in the last few years, with a number of landmark experimental demonstrations reporting effects caused by chiral phonons; including the phonon Hall effect, where a heat current is deflected in a magnetic field [4, 5]; the phonon Zeeman effect, where the degeneracy of left- and right-phonon states is lifted by the application of a magnetic field [6, 9, 10]; phonon analogues of the Einstein–de Haas effect [11–13]; the phonon Barnett effect, where a mechanical rotation causes change in magnetization (and vice versa) [14–17]; a report of the chiral phonon–activated spin-Seebeck effect, observed in a layered hybrid organic–inorganic perovskite implanted with chiral cations [18]; and thermal gradients used to drive transfer of angular momentum in the chiral insulator α-quartz [19, 20].

These intriguing experimental observations have stimulated theoretical work to understand how chiral phonon motion interacts with observable properties. These have included predictions that chiral phonons can induce currents in helical crystals [21], magnons in ferromagnets and antiferromagnets [22], drive spin magnetization [23], the chiral phonon–activated spin-Seebeck effect [24, 25], drive ultrafast spin dynamics in magnetic materials through magnonic rectification [26] and how chiral phonon modes can be driven by terahertz fields [27].

The spin-Seebeck effect [28, 29] is the spin-polarized version of the well-known Seebeck effect in thermoelectrics, where a thermal gradient can generate a (spin-polarized) current. This effect has given rise to the field of spin-caloritronics [30, 31]. A key application of this effect utilizes heating induced by femtosecond pulsed lasers to generate ultrafast spin current in ferromagnets, which can then be converted to a transverse charge current using the inverse spin-Hall effect. The ultrafast charge current gives rise to an electromagnetic field, which propagates in free space. The spectrum of these pulses typically falls in the terahertz frequency range. This has led to the rapid adoption of laser-driven spintronic emitters, based on the ultrafast spin-Seebeck effect, for terahertz pulse generation [32]. These emitters are typically formed of a thin ferromagnetic layer (e.g., Fe) to generate the spin-polarized current and a non-magnetic, heavy metal layer (e.g., Pt) to convert the spin current into a charge current, normal to both the spin current and the magnetization direction [33].

More generally, the generation of terahertz radiation upon exposure to ultrafast optical pulses has proven to be a powerful tool for non-destructively probing material properties. Known as terahertz emission spectroscopy (TES), the resulting radiated terahertz pulses are coherently detected in the time domain using electro-optic sampling techniques [34]. Applications include photocarrier dynamics in heterostructure p–n junctions [35], Rashba splitting in perovskite multiple quantum wells [36] and deconvolving bulk and surface effects in 3D topological insulators [37]. Furthermore, by adding a thin layer of heavy metal to perform spin-to-charge conversion, the same technique can probe spin dynamics on ultrafast timescales [38–40].

A promising candidate for chiral phonon applications is the layered semiconductor indium selenide (In_2Se_3) which can be grown by molecular beam epitaxy (MBE) [41, 42] and forms three main polymorphs, α, β, and γ [43, 44], exhibiting a range of physical and chemical properties, particularly ferroic, photovoltaic, and catalytic. Of these polymorphs, the layered α and β polymorphs have received particular attention because the α-phase was found to display out-of-plane ferroelectricity at room temperature [45, 46] and in-plane ferro/ferrielectric polarization has been reported in the β' phase at room temperature [47, 48].

Besides the typical applications of ferroelectricity, this finding also has implications for the study of chiral phonons, since hexagonal 2D materials are known to host cycloidal phonons at the Brillouin zone corners (K and K′) [7, 49]. While these axial phonons are considered achiral when the rules of 3D space are applied, the presence of broken mirror symmetry perpendicular to the plane of circular polarization, such as in ferroelectrics, can lead to cycloidal and Γ-point phonons breaking improper rotational symmetry. In this case, these phonon modes can be classified as exhibiting *false chirality* where either mirror reflection or time reversal can transform between the *left* and *right* states [3]. Crucially, this results in differing dispersions for left- and right-handed phonons, which is predicted to generate a finite angular momentum, inducing a magnetization in the sample when exposed to a temperature gradient [50, 51] and has more recently been predicted to induce a spin current in an adjacent metal [25].

These observations and predictions make ferroelectric films with in-plane polarization ideal materials for exploring and manipulating chiral phonons using ultrafast, out-of-plane temperature gradients. Room-temperature, in-plane ferroelectric polarization has been reported for β'–In_2Se_3, and DFT calculations have identified circular phonon modes in the closely related α-phase material [51]. Furthermore, large-area, high-quality films are available.

In this work, we study spin-current generation in an MBE-grown thick film of ferroelectric β'–In_2Se_3 by investigating the same film with and without a thin platinum layer. We observe signals consistent with ultrafast spin-current generation in a ferroelectric β'–In_2Se_3 film without an applied magnetic field or any magnetic materials, which we attribute to a chiral phonon–induced spin-Seebeck effect. This spin-current is converted to a charge current in the thin layer of heavy metal on the sample, the resulting terahertz field is measured, and polarization dependence is analyzed. This is the first experimental report of the ultrafast chiral phonon–activated spin-Seebeck effect in an inorganic material.

2 | Results

The sample consists of a 1 μm-thick film of In_2Se_3, deposited on a *c*-plane sapphire wafer by solid-source MBE. Approximately half of the wafer was then covered with a 3 nm-thick layer of platinum by DC sputtering, within the same vacuum system. This sample allows us to separate the effect of the thin Pt layer on the signal. The purpose of the Pt film is to convert a spin-current generated in the In_2Se_3 layer into a charge current orthogonal to both the direction and spin-polarization of that current, via the inverse spin-Hall effect. The In_2Se_3 film was characterized by a range of analytical techniques, including x-ray diffraction, Raman spectroscopy, and transmission electron microscopy (TEM), which confirmed that the film was β-phase In_2Se_3 with 3*R* stacking and the *c*-axis out-of-plane; SQUID magnetometry measurements confirmed there was no net magnetization present

15214095, 0, Downloaded from https://advanced.onlinelibrary.wiley.com/doi/10.1002/adma.75389 by NICE, National Institute for Health and Care Excellence, Wiley Online Library on [23/10/2026]. See the Terms and Conditions (https://onlinelibrary.wiley.com/terms-and-conditions) on Wiley Online Library for rules of use; OA articles are governed by the applicable Creative Commons License

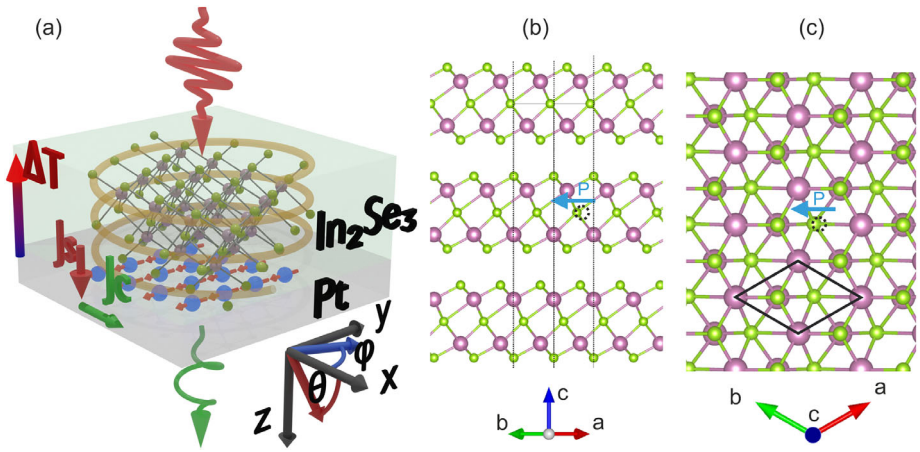


FIGURE 1 | (a) Schematic diagram of chiral phonon–mediated spin-Seebeck effect. A near-IR femtosecond pulse (show in red) generates a thermal gradient in the In_2Se_3 film, indicated by a red–blue fade. This temperature gradient gives rise to chiral phonons, circular motion of atoms indicated by orange spiral. This motion generates a spin current, J_s, red. On entering the Pt film this spin current is converted to a charge current, J_c, green, perpendicular to J_s via the inverse spin-Hall effect. This transient current gives rise to a THz field pulse emitted from the sample (green). (b) and(c) show the crystal structure of β'–In_2Se_3-3*R*, with purple spheres representing In and green for Se. (b) shows the 3*R* (ABC) layer stacking along the *c*-axis. The *c*-axis is parallel to the *z*-direction in our sample whereas the *a*- and *b*-axis are in-plane. The direction of the polarization is determined by the position of the central Se atom, indicated. (c) shows the view looking down the *c*-axis, with the central Se atom highlighted again.

in the sample. Comparing the Raman spectroscopy response to circularly polarized light with different handedness reveals a small polarization-dependent shift in the phonon peak at 110 cm^{-1} of 0.3 cm^{-1}, indicating chirality-dependent phonon dispersion is present in the sample [52]. We also performed piezo-force microscopy (PFM) on our sample, revealing an in-plane ferroelectric component, consistent with what has previously been observed for β'–In_2Se_3. The β'-phase of In_2Se_3 is a distorted version of the β-phase where the central selenium atom is displaced in-plane through spontaneous relaxation giving rise to ferro/ferrielectric polarization [47, 48, 53]. Further details of these techniques and additional data are given in the Methods and Suporting Information.

To generate a transient temperature gradient, the In_2Se_3/Pt sample was placed in the focus of a laser beam producing 100 fs pulses, with a center wavelength of 780 nm. Initially, the sample is illuminated through the sapphire substrate at normal incidence, ($\theta = 0°$, Figure 1), and the rotation of the sample (ϕ) adjusted to maximize the measured terahertz signal. The signal is proportional to the emitted electric field arriving at the detector and is measured by electro-optic sampling; further details are given in the Supporting Information, S4. Figure 2a shows the measured electric field as a function of time, together with the signal measured when the sample is rotated (ϕ) by 180°. The electric field recorded shows a near single-cycle pulse, with oscillations following the main peak, characteristic of a broadband electric-field pulse convolved with the ∼ 2.5THz bandwidth of the electro-optic sampling detection system. The observed flip in polarity with 180° rotation is not seen in ferromagnetic spintronic emitters, but is consistent with the symmetry of the ferroelectric polarization in the sample. The dependence of the signal maximum and minimum on the rotation angle, ϕ, summarized in Figure 2c, highlights this twofold symmetry and suggests that the direction of the ferroelectric polarization controls the emission. The in-plane ferroelectric domains observed in PFM data (Section S11) are on the order of 0.5 μm, smaller than the ∼20 μm spot size of the exciting pulse. Since no external bias is applied to the sample, it is likely that remanent polarization exists in the sample as a result of defects and/or strain [54, 55].

To determine the origin of the signal and specifically the role of the Pt film, we also measured the portion of the sample without the Pt film. When only the sapphire/In_2Se_3 is illuminated, the signal is significantly reduced, indicating the crucial role of the Pt in the generation mechanism and suggesting that the signal is not generated by a nonlinear optical process (such as optical rectification) in the $\beta' - In_2Se_3$. The sample was then tilted ($\theta > 0°$) and the dependence of the signals with and without the Pt layers on the tilt angle, θ, recorded; Figure 2d shows how the magnitude of each signal varies with tilt angle. When the Pt layer is present, the magnitude of the signal reduces as the tilt angle is increased, while the portion of the sample without the Pt film shows an increasing signal as the sample is tilted, this suggests two distinct generation mechanisms are present in the sample, dependent on tilt angle.

There are several reports of terahertz generation from materials sharing the same 3*m* point group as $\beta - In_2Se_3$ when illuminated with ultrafast laser pulses at 45° incidence [56]. There can be several contributions to this generation, dominated by ultrafast transient currents that combine contributions from photon drag [57]; photoconductive and thermoelectric effects [58]; and, more recently, a report that shift currents are the dominant generation mechanism in $\alpha - In_2Se_3$ at oblique incidence [59]. However, all of these require an oblique angle of incidence to produce a net in-plane ultrafast current that produces the terahertz pulse; this cannot explain the signal measured from the In_2Se_3/Pt sample at normal incidence.

To understand the origin of the measured signal, we investigate how the emitted electric field changes when the femtosecond pulse excites the sample from the opposite side; the comparison is shown in Figure 3a. A delay in time of the peak signal appears

15214095, 0, Downloaded from https://advanced.onlinelibrary.wiley.com/doi/10.1002/adma.75389 by NICE, National Institute for Health and Care Excellence, Wiley Online Library on [23/10/2026]. See the Terms and Conditions (https://onlinelibrary.wiley.com/terms-and-conditions) on Wiley Online Library for rules of use; OA articles are governed by the applicable Creative Commons License

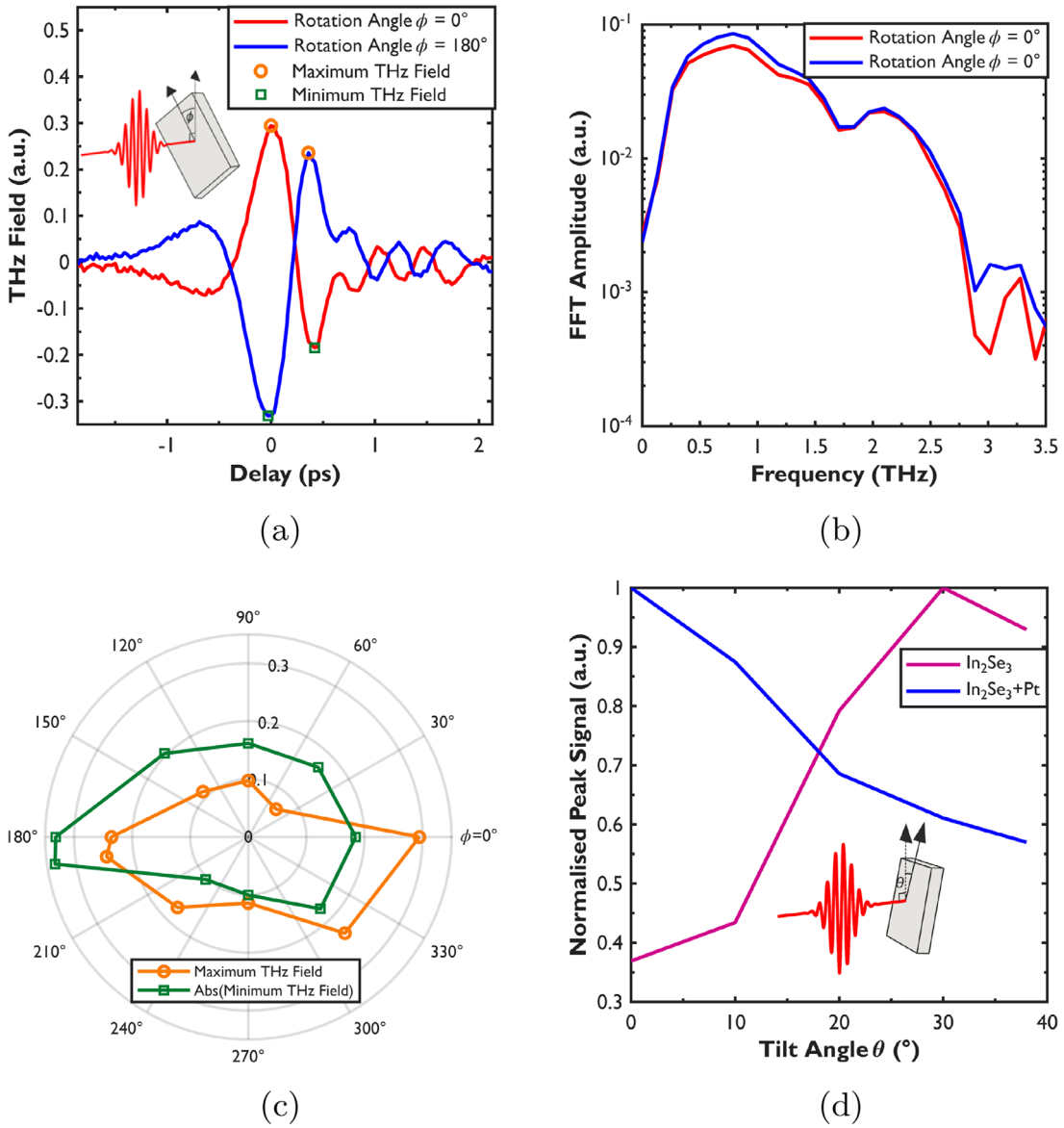


FIGURE 2 | (a) Terahertz electric field pulses generated from In_2Se_3/Pt with a 780 nm pump pulse with 850 mW optical power. (b) Fourier transform of the time-domain responses in (a). Roll-off of the response around 2.5 THz is from limited bandwidth of the ZnTe detection crystal. (c) Peak Terahertz field generated from In_2Se_3/Pt as a function of sample rotation (ϕ), indicated in (a). (d) Peak time-domain response of the terahertz pulses emitted from In_2Se_3/Pt and In_2Se_3 at different tilt angles (θ), indicated by the inset. The response from the In_2Se_3 increases as the tilt angle gets closer to 45°, whilst the response from In_2Se_3/Pt decreases, indicating that the main generation mechanism of In_2Se_3/Pt is not a nonlinear optical effect.

when the pulse enters through the Pt layer because the terahertz pulse generated in the sample now travels through the sapphire substrate instead of the 780 nm pump pulse. There is a large difference in the refractive index of sapphire between these two wavelengths (1.76 at near-infrared vs. ~ 3.1 in the terahertz region [60]). The reduction in intensity between the two terahertz pulses is most likely due to a large proportion of the pump beam being reflected from the Pt face. The key difference here is that when the direction of excitation is reversed, the sign of the measured electric field is also reversed because the sign of the spin-current, j_s, is reversed. This is not observed in most terahertz emitters, such as photoconductive devices where the polarity of the emitted pulse is dictated by an applied electric field, but does mirror what is observed in "spintronic" terahertz emitters. In those emitters, the femtosecond pulses excite electrons in the ferromagnetic (FM) film from the spin polarized *d*-bands to *s*-bands, which, together with the different transport properties of the FM and normal metal (NM) layers, generates a large spin-polarized charge current along the *z*-direction. This is converted to an orthogonal charge current via the inverse spin-Hall in the normal metal (NM) layer. The resulting charge current, $\mathbf{j}_c$ can be written as

$$\mathbf{j}_c = \Theta_{SH}\frac{2e}{\hbar}(\mathbf{j}_s(t) \times \hat{\boldsymbol{\sigma}}(t)) \quad (1)$$

where Θ_{SH} is the spin-Hall angle, $\mathbf{j}(t)_s$ is the spin current, and $\hat{\boldsymbol{\sigma}}$ is the unit vector indicating the spin-polarization direction.

When the sample is reversed, the direction of the spin current (FM → NM) also reverses, which causes a change in sign of $\mathbf{j}_s$

15214095, 0, Downloaded from https://advanced.onlinelibrary.wiley.com/doi/10.1002/adma.75389 by NICE, National Institute for Health and Care Excellence, Wiley Online Library on [23/10/2026]. See the Terms and Conditions (https://onlinelibrary.wiley.com/terms-and-conditions) on Wiley Online Library for rules of use; OA articles are governed by the applicable Creative Commons License

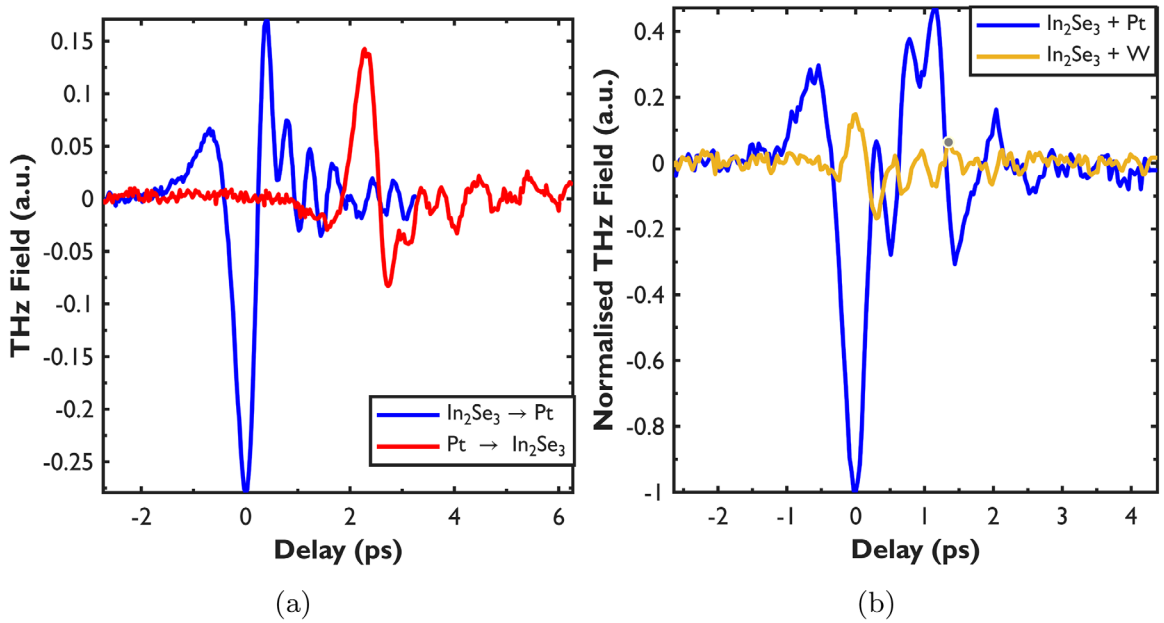


FIGURE 3 | (a) Time-domain responses ($\theta = 0°$, $\phi = 180°$) of the terahertz pulses emitted from In_2Se_3/Pt when the pump beam enters the In_2Se_3 or Pt layer first, causing a flip in pulse polarity. Sample pumped with 850 mW optical power. (b) Time-domain responses of the terahertz pulses emitted from In_2Se_3/Pt and In_2Se_3/W, pumped with 600 mW optical power. A flip in the THz pulse's polarization is observed, caused by the flip in sign of the metal layer's spin-Hall angle (positive for Pt and negative for W).

and flip in the polarity of the resulting electric field generated by $\mathbf{j}_c$. In the present case, our observation suggests a similar generation mechanism, with emission resulting from a current entering the Pt film from the β'–In_2Se_3. The dependence on the emitted terahertz field to the optical pump power was also found to be linear, as expected from similar generation mechanisms (shown in Supporting Information S6).

To determine the type of current flowing between the layers and test if the inverse spin-Hall effect in the Pt layer is part of the generation mechanism, a portion of the same sample was coated with tungsten (W). This resulted in a single piece of sapphire substrate with three regions; In_2Se_3/Pt, In_2Se_3, and In_2Se_3/W. Tungsten was chosen because it has a spin-Hall conductivity with an opposite sign to that of Pt; Pt has a spin-Hall conductivity of 4.2e5 Sm^{-1}, whereas W has a spin-Hall conductivity of −1.8e5 Sm^{-1} [61].

The sample emission is shown in Figure 3b and a flip in the electric field polarity is seen when the Pt is replaced with W, as well as a reduction in the magnitude of the peak field. While a reduction in the generated field is expected from the reduced magnitude of Θ_{SH} in W, the reduction is larger than might be expected. We ascribe this to the fact that the In_2Se_3 surface was exposed to atmosphere before the deposition of W, possibly degrading the interface, while the Pt was deposited without exposure to atmosphere. These measurements suggest that a transient spin-current is flowing into the metal layer, and being converted into a transient charge current via the ISHE. While heavy metal layers can also facilitate orbital-to-charge conversion and other interfacial current generation processes as the induced angular momentum may contain orbital spin-current, orbital-current, or mixed spin/orbital-current components [20, 62, 63], our observations of a flip in polarization suggest that spin-Hall conversion dominates over an orbital contribution (Pt and W have spin-Hall conductivities of opposite sign, whereas their orbit-Hall conductivities have the same sign [64]). Moreover, previous studies of terahertz emission from orbit-Hall conversion in devices with a heavy metal overlayer observe a change in the timing of the emission when switching from Pt and W, ascribed to the different propagation velocities of the spin and orbital currents in the heavy metal layer [62]; no change in timing is observed from the results presented here, leading us to conclude that the ISHE is the primary emission mechanism.

Although SQUID magnetometry measurements indicated that there is no magnetization, and In_2Se_3 is not a magnetic material, we also verified the dependence of the emitted signal on an applied magnetic field. A pair of permanent neodymium magnets was placed on either side of the sample, providing a static external magnetic field with the field direction in the plane of the sample, estimated to be 50 mT. The presence of the external magnetic field applied did not induce any measurable change in the terahertz pulses produced from the In_2Se_3/Pt sample. Together, these measurements provide strong evidence for spin-current generation in the non-magnetic β'–In_2Se_3 film that is consistent with a spin-Seebeck-type mechanism, which we attribute to chiral-phonon activation.

We next investigate the polarization of the emitted terahertz pulse and the dependence of this on the polarization of the pump pulse exciting the sample. Figure 4 plots the polarization-resolved emission from the sample when the linearly polarized excitation pulse is (a) horizontally polarized and (b), rotated by 120° (while the sample remains fixed). Figure 4c plots field magnitude as a function of excitation polarization, together with the polarization ellipses of the emitted terahertz pulse at the peak emission frequency (0.65THz). The figures show that the emitted THz

15214095, 0, Downloaded from https://advanced.onlinelibrary.wiley.com/doi/10.1002/adma.75389 by NICE, National Institute for Health and Care Excellence, Wiley Online Library on [23/10/2026]. See the Terms and Conditions (https://onlinelibrary.wiley.com/terms-and-conditions) on Wiley Online Library for rules of use; OA articles are governed by the applicable Creative Commons License

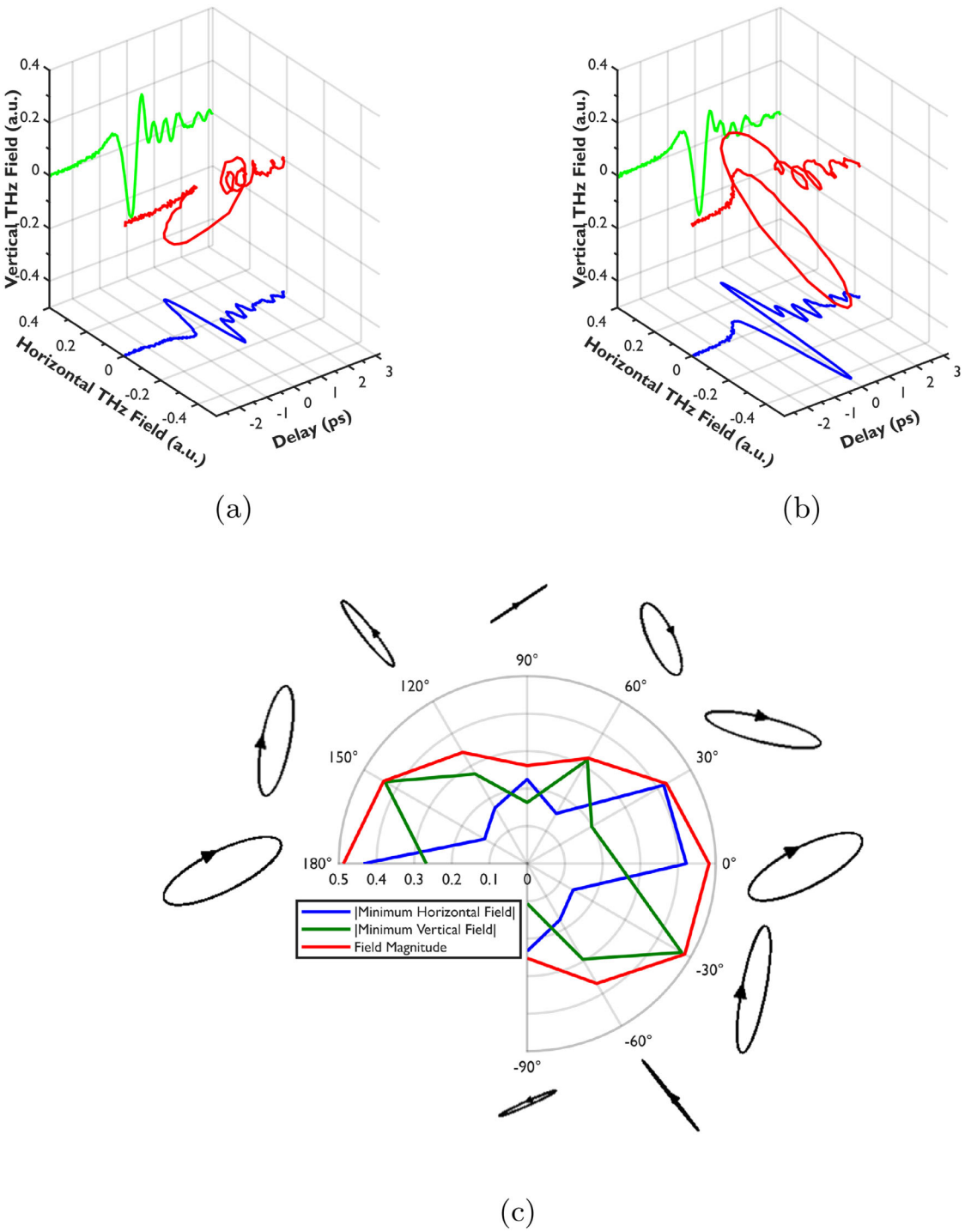


FIGURE 4 | (a) Left-handed circularly polarized terahertz pulse generated from the In_2Se_3/Pt with a horizontally polarized IR pump (180° rotation). (b) Right-handed circularly polarized terahertz pulse generated from the sample when the IR pump polarization is rotated by 120°. (c) The peak field magnitude of the generated terahertz pulses as a function of the IR pump pulse polarization rotation. The sample was pumped with 850 mW optical power for all these measurements. Polarization ellipses of the generated terahertz pulses at 0.65 THz shown on the exterior of the graph.

pulse has a significant circular component to the emission, which depends on the polarization of the excitation pulse; the emission is clearly left-handed elliptically polarized when the excitation is horizontally polarized (0° and 180°, Figure 4a), whereas the emission is weakly right-handed elliptically polarized when the polarization of the excitation pulse is at 120° and, to a lesser extent, at −90° (e.g., Figure 4b). Between these, the emission becomes purely linearly polarized, most notably at 90°. The time-domain plots for each pump polarization angle and details of the calculation of the polarization ellipses can be found in Sections S7 and S8.

Figure 4c shows that the polarization of the emitted pulse has a clear dependence on the polarization direction of the exciting pulse. These results echo the twofold symmetry in the emission

15214095, 0, Downloaded from https://advanced.onlinelibrary.wiley.com/doi/10.1002/adma.75389 by NICE, National Institute for Health and Care Excellence, Wiley Online Library on [23/10/2026]. See the Terms and Conditions (https://onlinelibrary.wiley.com/terms-and-conditions) on Wiley Online Library for rules of use; OA articles are governed by the applicable Creative Commons License

observed when rotating the sample (Figure 2), indicating that not only the magnitude of the signal, but also the ellipticity of the emission displays twofold symmetry. This is likely linked to the ferroelectric polarization, observed with PFM (see Methods and Section S11). These results are in contrast to the behavior of ferromagnetic spintronic emitters where the polarization of the generated pulse depends only on the direction of the applied magnetic field (see Section S5, for a comparison). Furthermore, in the few theoretical treatments of the chiral phonon–activated spin-Seebeck effect, the polarization of the exciting pulse is not considered; the only stimulation is a temperature gradient. The complex dependence of the emission polarization on the excitation polarization observed here suggests that there are additional contributions to the terahertz emission in this case.

Furthermore, because the excitation and detection are normal to the sample surface, the emission mechanism is expected to be mediated by the inverse spin-Hall effect Equation (1). If this is the dominant terahertz emission mechanism, it can be linked to an induced spin-current. The generated THz field is proportional to the differential in time of the transient current flowing in the plane of the sample, perpendicular to the emission direction. Therefore, our results imply that the spin current entering the Pt film has a time-dependent polarization direction, with a handedness that can be controlled by direction of incident IR pulse polarization, relative to the sample orientation. Expressions describing how the emitted terahertz field depends on the time-dependent spin-current magnitude and spin-polarization vector are derived in Section S10, together with the results of fitting these expressions to the data to extract the spin current magnitude and polarization.

3 | Discussion

These results show clearly that an optically generated spin current (probed using THz emission spectroscopy in a heavy metal) can be stimulated in non-magnetic β'–In_2Se_3. We interpret these observations as arising from a chiral phonon–mediated spin-Seebeck effect, given that (1) magnetization is neither predicted nor observed in our β'–In_2Se_3 sample; (2) the material is ferroelectric and predicted to show different dispersions for different phonon chiralities; and, (3) the theoretical predictions of a phonon angular momentum perpendicular to both the thermal gradient and ferroelectric polarization. The theoretical analysis presented in refs. [25, 50, 51] shows that a thermal gradient induced in a material with different dispersions for different phonon chiralities (for example, by a transient heating), gives rise to a phonon angular momentum and transient magnetization perpendicular to both the thermal gradient and the electric polarization of the sample. For our sample, where the thermal gradient is applied in the z-direction, perpendicular to the plane of the sample, and a ferroelectric polarization, which lies in the plane of the sample, the transient magnetization will also lie in the plane of the sample (this is described in more detail in Section S9). This transient magnetization, derived from the chiral-phonon atomic micro-rotations, will induce a spin current at the interface with the heavy metal [65]. It is this spin current, which generates the terahertz emission via the ISHE.

However, these models do not explain all the features of the emission that we observe. In particular, neither the dependence on the polarization state of the excitation pulse, nor the observed elliptically polarized emission. Given our observation of the dependence of the emission polarization on the excitation polarization, these features are clearly linked. One explanation for this observation could be ultrafast "shift currents" generated by the linear bulk photovoltaic effect, which reference [59] determined to be the dominant ultrafast current source when excited with a femtosecond laser at oblique incidence in α–In_2Se_3. That work found incident pulses generated transient shift-currents in the material, which led to transient terahertz pulses with both x- and y- components. While these cannot directly explain the terahertz emission at normal incidence that we see here, because, at normal incidence, symmetry considerations prohibit a net in-plane current, these currents do exhibit strong dependence on the excitation pulse polarization and can give rise to elliptically polarized emission. We suggest that shift currents driven perpendicular to the plane of the sample could become spin-polarized by the local transient magnetization induced by the chiral phonons [23]. This spin-polarized current could then contribute to the emission observed in this work. Further theoretical and experimental investigations will be required to establish the precise microscopic mechanism. For example, the dependence on β'–In_2Se_3 thickness on the generation could be studied, or to assess the role of photo-generated carriers, a layer of metal (e.g., Al) could be added to the sample, with the aim of blocking the femtosecond pulse, while still allowing for rapid heating.

Beyond the fundamental interest in the role of chiral phonons in spin current generation in non-magnetic materials, our results also highlight the power of using the inverse spin-Hall effect coupled with polarization-resolved terahertz emission spectroscopy to investigate ultrafast spin-currents. This is achieved by adding a thin heavy metal layer to convert the generated spin-current into an orthogonal charge current and using polarization resolved detection to provide a rich time-resolved dataset, which depends directly on the spin-current polarization.

The findings presented here could also be relevant for applications in terahertz spectroscopy; for example, in circular dichroism spectroscopy, a technique particularly useful for complex molecules, which often show distinct responses in linear THz spectroscopy. The implementation of this technique has been challenging in the terahertz region, owing to the lack of compact broadband terahertz emitters capable generating circularly polarized light. While this application has stimulated the engineering of terahertz emitters [66, 67] to emit circularly polarized light, the results presented here suggest that β'–In_2Se_3 and related materials could provide an appealing alternative, showing intrinsic elliptically polarized emission. Furthermore, the circularity of the emission can be controlled by changing the polarization of the input pulse, as shown here, or potentially by electrically switching the ferroelectric domains [51]. The ability to rapidly switch polarization is particularly appealing for circular dichroism spectroscopy to determine small differences in the response to different polarizations for chiral molecules. Additionally, the observation that the spot size of the optical excitation is significantly larger than the ferroelectric domains

15214095, 0, Downloaded from https://advanced.onlinelibrary.wiley.com/doi/10.1002/adma.75389 by NICE, National Institute for Health and Care Excellence, Wiley Online Library on [23/10/2026]. See the Terms and Conditions (https://onlinelibrary.wiley.com/terms-and-conditions) on Wiley Online Library for rules of use; OA articles are governed by the applicable Creative Commons License

suggest that by poling the sample, the magnitude of the signal could also be increased.

Finally, the measurements reported here suggest that other effects predicted in this material, β'–In_2Se_3, could be observable. This includes effects such as thermally induced phonon magnetization, the phonon Hall effect and interface phonon modes at domain boundaries. Combined with scalable large-area growth techniques, these properties make the material readily compatible with device integration, opening the prospect of device engineering for advanced phononic and spintronic applications.

4 | Methods

4.1 | Sample Details

The sample was grown on a 500 μm thick $< 0001 >$ sapphire substrate using solid-source molecular beam epitaxy (MBE), at a base pressure of $\simeq$ 4e10 mbar, by co-deposition of selenium and indium, evaporated from standard dual-filament Knudsen cells, resulting in a 1 μm thick film of In_2Se_3. The growth procedure followed the method described in Ref [68]. Initially a 3 nm Bi_2Se_3 seed layer was deposited at 130°C, followed by a 10 nm In_2Se_3 layer at 300°C (growth rate of $\sim$0.3 nm/min). To achieve high crystallinity, the sample was annealed at 600°C for 1 h; during this process, the Bi_2Se_3 layer was evaporated from the wafer [68]. The temperature was then reduced to 300°C to complete the growth of a $\sim$1 μm thick In_2Se_3 film at a rate of 0.9 nm/min. The sample was cooled to 130°C under a Selenium atmosphere. After cooling, the sample was transferred under vacuum to a different growth chamber for Pt deposition by DC sputtering. Half of the wafer was shadow masked before being sputtered with a thin layer of platinum (3 nm thickness), providing a region of In_2Se_3 and a region of In_2Se_3/Pt.

4.2 | X-Ray Diffraction

X-Ray diffraction (XRD) measurements, performed using Cu Kα radiation, indicate that the c-axis of the In_2Se_3 is perpendicular to the growth direction. The extracted lattice constant in this direction, 28 Å, is consistent with both α and β phases of In_2Se_3, which exhibit $R3m$ and $R\bar{3}m$ structures respectively from the layer stacking of Se–In–Se–In–Se, with the bond angle between the stacked layers of In and Se changing slightly between the two phases [42, 44]. The XRD data is presented in Section S1.

4.3 | Optical Excitation and Electric Field Detection

The experimental system used to generate and detect the terahertz radiation produced from the samples was pumped with a Ti:Sapphire laser (SpectraPhysics MaiTai) with 80 MHz repetition rate, 780 nm center wavelength and 100 fs pulse width. A 2 nm thick ZnTe crystal was used to detect the terahertz pulses using electro-optic sampling, giving a detection bandwidth of 2.5THz. A PTFE filter was placed between the emitter and detection crystal to block the excess pump beam that is not absorbed in the sample. Compared to standard terahertz emission spectroscopy, extra optics have been added to allow for detection of both horizontally and vertically polarized terahertz radiation, namely a half-waveplate and Glan–Taylor polarizer in the sampling beam to rotate the polarization of the detection pulse and a wiregrid polarizer to selectively allow either the horizontally or vertically polarized terahertz pulses to reach the detection crystal. The detection crystal is also rotated to ensure maximum detection efficiency for each polarization state. Details of the polarization-detection characterization can be found in Section S4.

4.4 | Circularly Polarized Raman Spectroscopy

A Horiba LabRam HR800 Raman microscope with a red laser of wavelength 632.8 nm, a ×100 objective lens, and a grating with 1800 lines/mm was used to perform the Raman spectroscopy measurements of the In_2Se_3 sample. A linear polarizer and a rotatable $\frac{\lambda}{4}$ waveplate were placed before the objective lens to circularly polarize the pump with either left- or right-handedness. Raman data is presented in Section S3.

4.5 | Piezo Force Microscopy

Piezo Force Microscopy (PFM) was performed using an Asylum MFD 3D Infinity system, with PtIr-coated Si AFM tips. An AC bias of magnitude 4V was applied with a frequency close to the resonance frequency of the cantilevers, approximately 300kHz for the out of plane (vertical) mapping, and 650 kHz for the in-plane response. PFM data is presented in Section S11.

4.6 | Transmission Electron Microscopy

A FEI Helios G4 DualBeam Focused Ion Beam Scanning Electron Microscope (FIBSEM), at an accelerating voltage of 30kV, was used to prepare an electron-transparent lamella of In_2Se_3 for cross-sectional imaging in the Transmission Electron Microscope (TEM). We used an FEI Titan3 Themis 300 operating at 300kV in TEM mode to produce the lattice and diffraction images.

The diffraction pattern indexing was performed using a Crystal Maker3 Single Crystal workflow using a CIF simulation of the $\alpha - 3R$ and $\beta - 3R$ In_2Se_3 phases to produce an indexed pattern with the same orientation as the measurement. Further data are presented in Section S2.

4.7 | SQUID Magnetometry

The magnetic moment of samples diced into 4 nm squares was measured using a Quantum Design MPMS3 system in vibrating sample magnetometry mode. This measurement protocol has a sensitivity of approximately 1e-8 emu. When measured with an external field of 500 mT at room temperature, only a linear dependence of the moment is seen, typical of the overall diamagnetic background of the sapphire substrate, indicating that there is no intrinsic magnetism in the film.

15214095, 0, Downloaded from https://advanced.onlinelibrary.wiley.com/doi/10.1002/adma.75389 by NICE, National Institute for Health and Care Excellence, Wiley Online Library on [23/10/2026]. See the Terms and Conditions (https://onlinelibrary.wiley.com/terms-and-conditions) on Wiley Online Library for rules of use; OA articles are governed by the applicable Creative Commons License

Author Contributions

J.R.F. and S.D. conceived the project; J.R.F., S.D., and E.H.L acquired funding; A.Y. and M.R. grew the sample under the supervision of S.S. and B. H; M.R. performed SQUID magnetometry measurements; A.Y. measured x-ray diffraction from the samples; B.M. and Z.A. measured electron microscopy under the supervision of T.M.; C.J.M., and J.M.G. measured and analyzed piezo force microscopy data; L.B. and O.C. measured and analyzed the Raman spectroscopy data; T.B.G. measured and analyzed terahertz emission spectroscopy data with assistance from P.R., N.F., and J.R.F.; T.B.G. and J.R.F. wrote the initial manuscript draft; J.R.F. supervised the overall research; All authors discussed the results and contributed to the final version of the manuscript.

Acknowledgments

The authors gratefully acknowledge the support of the LEMAS facility at the University of Leeds for their assistance with the Transmission Electron microscopy.

Funding

This work was supported financially by the UK research and innovation councils through the grant NAME (EP/V001914/1) and CAMIE (EP/X027074/1) as well as by the European Union through the project EXTREME-IR (EU project:964735). T.M. was supported by the Royal Academy of Engineering through Fellowship number RF/201920/19/245. The samples were grown in the Royce Deposition system at the University of Leeds, which is supported by the Henry Royce Institute, UK, through the grants EP/P022464/1 and EP/R00661X/1.

Conflicts of Interest

The authors declare no conflicts of interests.

Data Availability Statement

The data associated with this paper are publicly available from the University of Leeds Data Repository at https://doi.org/10.5518/1837. The thin-film samples used in this study were custom grown in our laboratory using deposition conditions described in the Methods section. These films are not commercially available. Due to limitations in fabrication capacity and sample stability, only a limited number of thin-film samples can be provided by the corresponding author upon reasonable request and subject to a material transfer agreement. Scripts for data analysis are available from the University of Leeds Data Repository at https://doi.org/10.5518/1837.

References

1. H. Ueda, M. García-Fernández, S. Agrestini, et al., "Chiral Phonons in Quartz Probed by X-Rays," *Nature* 618, no. 7967 (2023): 946–950, https://doi.org/10.1038/s41586-023-06016-5.

2. K. Ishito, H. Mao, K. Kobayashi, et al., "Chiral Phonons: Circularly Polarized Raman Spectroscopy and Ab Initio Calculations in a Chiral Crystal Tellurium," *Chirality* 35, no. 6 (June 2023): 338–345, https://doi.org/10.1002/chir.23544.

3. D. M. Juraschek, R. M. Geilhufe, H. Zhu, et al., "Chiral Phonons," *Nature Physics* 21 (2025): 1532–1540, https://doi.org/10.1038/s41567-025-03001-9.

4. G. Grissonnanche, A. Legros, S. Badoux, et al., "Giant Thermal Hall Conductivity in the Pseudogap Phase of Cuprate Superconductors," *Nature* 571, no. 7765 (2019): 376–380, https://doi.org/10.1038/s41586-019-1375-0.

5. X. Li, B. Fauqué, Z. Zhu, and K. Behnia, "Phonon Thermal Hall Effect in Strontium Titanate," *Physical Review Letters* 124, no. 10 (2020): 105901, https://doi.org/10.1103/PhysRevLett.124.105901.

6. F. Wu, S. Bao, J. Zhou, et al., "Fluctuation-Enhanced Phonon Magnetic Moments in a Polar Antiferromagnet," *Nature Physics* 19, no. 12 (2023): 1868–1875, https://doi.org/10.1038/s41567-023-02210-4.

7. H. Zhu, J. Yi, M.-Y. Li, et al., "Observation of Chiral Phonons," *Science* 359, no. 6375 (2018): 579–582, https://doi.org/10.1126/science.aar2711.

8. H. Sun, T. Wang, Z. Chen, et al., "The Rise of Chiral Phononics: From Fundamental Concepts to Emergent Quasiparticle Interactions," *Physics Reports* 1195 (2026): 1–99, https://doi.org/10.1016/j.physrep.2026.07.002.

9. B. Cheng, T. Schumann, Y. Wang, et al., "A Large Effective Phonon Magnetic Moment in a Dirac Semimetal," *Nano Letters* 20, no. 8 (2020): 5991–5996.

10. F. G. Hernandez, A. Baydin, S. Chaudhary, et al., "Observation of Interplay Between Phonon Chirality and Electronic Band Topology," *Science Advances* 9, no. 50 (2023): eadj4074, https://doi.org/10.1126/sciadv.adj4074.

11. C. Dornes, Y. Acremann, M. Savoini, et al., "The Ultrafast Einstein–de Haas Effect," *Nature* 565, no. 7738 (2019): 209–212, https://doi.org/10.1038/s41586-018-0822-7.

12. S. R. Tauchert, M. Volkov, D. Ehberger, et al., "Polarized Phonons Carry Angular Momentum in Ultrafast Demagnetization," *Nature* 602, no. 7895 (2022): 73–77, https://doi.org/10.1038/s41586-021-04306-4.

13. L. Zhang and Q. Niu, "Angular Momentum of Phonons and the Einstein–de Haas Effect," *Physical Review Letters* 112, no. 8 (2014): 085503.

14. T. F. Nova, A. Cartella, A. Cantaluppi, et al., "An Effective Magnetic Field From Optically Driven Phonons," *Nature Physics* 13, no. 2 (2017): 132–136, https://doi.org/10.1038/nphys3925.

15. D. M. Juraschek, T. Neuman, and P. Narang, "Giant Effective Magnetic Fields From Optically Driven Chiral Phonons in 4f Paramagnets," *Physical Review Research* 4, no. 1 (2022): 013129, https://doi.org/10.1103/PhysRevResearch.4.013129.

16. M. Basini, M. Pancaldi, B. Wehinger, et al., "Terahertz Electric-Field-Driven Dynamical Multiferroicity in $SrTiO_3$," *Nature* 628, no. 8008 (2024): 534–539, https://doi.org/10.1038/s41586-024-07175-9.

17. C. S. Davies, F. G. N. Fennema, A. Tsukamoto, I. Razdolski, A. V. Kimel, and A. Kirilyuk, "Phononic Switching of Magnetization by the Ultrafast Barnett Effect," *Nature* 628, no. 8008 (2024): 540–544, https://doi.org/10.1038/s41586-024-07200-x.

18. K. Kim, E. Vetter, L. Yan, et al., "Chiral-Phonon-Activated Spin Seebeck Effect," *Nature Materials* 22, no. 3 (2023): 322–328, https://doi.org/10.1038/s41563-023-01473-9.

19. K. Ohe, H. Shishido, M. Kato, S. Utsumi, H. Matsuura, and Y. Togawa, "Chirality-Induced Selectivity of Phonon Angular Momenta in Chiral Quartz Crystals," *Physical Review Letters* 132 (2024): 056302, https://doi.org/10.1103/PhysRevLett.132.056302.

20. Y. Nabei, C. Yang, H. Sun, et al., "Orbital Seebeck Effect Induced by Chiral Phonons," *Nature Physics* 22 (2026): 245–251, https://doi.org/10.1038/s41567-025-03134-x.

21. D. Yao and S. Murakami, "Chiral-Phonon-Induced Current in Helical Crystals," *Physical Review B* 105, no. 18 (2022): 184412, https://doi.org/10.1103/PhysRevB.105.184412.

22. D. Yao and S. Murakami, "Conversion of Chiral Phonons into Magnons in Ferromagnets and Antiferromagnets," *Journal of the Physical Society of Japan* 93, no. 3 (2024): 034708, https://doi.org/10.7566/JPSJ.93.034708.

23. D. Yao and S. Murakami, "Theory of Spin Magnetization Driven by Chiral Phonons," *Physical Review B* 111, no. 13 (2025): 134414, https://doi.org/10.1103/PhysRevB.111.134414.

24. X. Li, J. Zhong, J. Cheng, et al., "Chiral Phonon Activated Spin Seebeck Effect in Chiral mazterials," *Science China Physics, Mechanics & Astronomy* 67, no. 3 (2024): 237511, https://doi.org/10.1007/s11433-023-2281-x.

15214095, 0, Downloaded from https://advanced.onlinelibrary.wiley.com/doi/10.1002/adma.75389 by NICE, National Institute for Health and Care Excellence, Wiley Online Library on [23/10/2026]. See the Terms and Conditions (https://onlinelibrary.wiley.com/terms-and-conditions) on Wiley Online Library for rules of use; OA articles are governed by the applicable Creative Commons License

25. N. Nishimura, T. Funato, M. Matsuo, and T. Kato, "Theory of spin Seebeck Effect Activated by Acoustic Chiral Phonons," *Journal of Magnetism and Magnetic Materials* 630 (2025): 173386, https://doi.org/10.1016/j.jmmm.2025.173386.

26. T. Kahana, D. A. B. Lopez, and D. M. Juraschek, "Light-Induced Magnetization From Magnonic Rectification," *Science Advances* 10 (2024): 722, https://doi.org/10.1126/sciadv.ado0722.

27. H. Sun, X. Li, and L. Zhang, "Finite-Temperature Green's Function Theory of Terahertz-Induced Phonon Angular Momentum in Polar Crystals," *Physical Review B* 114, no. 15 (2026): 154303, https://doi.org/10.1103/ysd2-6ch2.

28. K. Uchida, S. Takahashi, K. Harii, et al., "Observation of the Spin Seebeck Effect," *Nature* 455, no. 7214 (2008): 778–781, https://doi.org/10.1038/nature07321.

29. K. Uchida, H. Adachi, T. An, et al., "Long-Range Spin Seebeck Effect and Acoustic Spin Pumping," *Nature Materials* 10, no. 10 (2011): 737–741, https://doi.org/10.1038/nmat3099.

30. G. E. W. Bauer, E. Saitoh, and B. J. Van Wees, "Spin Caloritronics," *Nature Materials* 11, no. 5 (2012): 391–399, https://doi.org/10.1038/nmat3301.

31. T. Liu, J. Peiro, D. K. De Wal, J. C. Leutenantsmeyer, M. H. D. Guimarães, and B. J. Van Wees, "Spin caloritronics in a $CrBr_3$-Based Magnetic van der Waals Heterostructure," *Physical Review B* 101, no. 20 (2020): 205407, https://doi.org/10.1103/PhysRevB.101.205407.

32. E. T. Papaioannou and R. Beigang, "THz Spintronic Emitters: A Review on Achievements and Future Challenges," *Nanophotonics* 10, no. 4 (2021): 1243–1257, https://doi.org/10.1515/nanoph-2020-0563.

33. M. Wang, Y. Zhang, L. Guo, M. Lv, P. Wang, and X. Wang, "Spintronics Based Terahertz Sources," *Crystals* 12, no. 11 (2022): 1661, https://doi.org/10.3390/cryst12111661.

34. Y. Wu, Y. Wang, D. Bao, et al., "Emerging Probing Perspective of Two-Dimensional Materials Physics: Terahertz Emission Spectroscopy," *Light: Science & Applications* 13, no. 1 (2024): 146, https://doi.org/10.1038/s41377-024-01486-2.

35. F. Murakami, K. Serita, I. Kawayama, et al., "Probing photocarrier dynamics in a Bi_2Te_3–Te Eutectic p–n Junction With a Laser Terahertz Emission Microscope," *APL Materials* 11, no. 3 (2023): 031102, https://doi.org/10.1063/5.0137862.

36. X. Liu, A. Chanana, U. Huynh, et al., "Circular Photogalvanic Spectroscopy of Rashba Splitting in 2D Hybrid Organic–Inorganic Perovskite Multiple Quantum Wells," *Nature Communications* 11, no. 1 (2020): 323, https://doi.org/10.1038/s41467-019-14073-6.

37. A. Nivedan and S. Kumar, "Excitation Wavelength-Dependent Ultrafast THz Emission From Surface and Bulk of Three-Dimensional Topological Insulators," *Journal of Physics D: Applied Physics* 56, no. 25 (2023): 255101, https://doi.org/10.1088/1361-6463/ACCBCB.

38. M. Mičica, A. Wright, S. Massabeau, et al., "Terahertz Electronic and Spin Currents in Wafer-Scale Van der Waals $Bi2Se_3/WSe_2$ Heterostructures and Polymorphs," *Advanced Materials* 38, no. 1 (2026): e06031, https://doi.org/10.1002/adma.202506031.

39. J. Hawecker, E. Rongione, A. Markou, et al., "Spintronic THz Emitters Based on Transition Metals and Semi-Metals/Pt Multilayers," *Applied Physics Letters* 120, no. 12 (2022): 122406, https://doi.org/10.1063/5.0079955.

40. E. Rongione, L. Baringthon, D. She, et al., "Spin-Momentum Locking and Ultrafast Spin-Charge Conversion in Ultrathin Epitaxial $Bi_{1-x}Sb_x$ Topological Insulator," *Advanced Science* 10, no. 19 (2023): 2301124, https://doi.org/10.1002/advs.202301124.

41. G. Han, Z. Chen, J. Drennan, and J. Zou, "Indium Selenides: Structural Characteristics, Synthesis and Their Thermoelectric Performances," *Small* 10, no. 14 (2014): 2747–2765, https://doi.org/10.1002/smll.201400104.

42. M. Küpers, P. M. Konze, A. Meledin, et al., "Controlled Crystal Growth of Indium Selenide, In_2Se_3, and the Crystal Structures of α-In_2Se_3," *Inorganic Chemistry* 57, no. 18 (2018): 11775–11781, https://doi.org/10.1021/acs.inorgchem.8b01950.

43. L. Liu, J. Dong, J. Huang, et al., "Atomically Resolving Polymorphs and Crystal Structures of In_2Se_3," *Chemistry of Materials* 31, no. 24 (2019): 10143–10149, https://doi.org/10.1021/acs.chemmater.9b03499.

44. C. K. Y. Tan, W. Fu, and K. P. Loh, "Polymorphism and Ferroelectricity in Indium(III) Selenide," *Chemical Reviews* 123, no. 13 (2023): 8701–8717, https://doi.org/10.1021/acs.chemrev.3c00129.

45. W. Ding, J. Zhu, Z. Wang, et al., "Prediction of intrinsic two-dimensional ferroelectrics in In_2Se_3 and other III_2-VI_3 van der Waals Materials," *Nature Communications* 8, no. 1 (2017): 14956, https://doi.org/10.1038/ncomms14956.

46. F. Xue, W. Hu, K. Lee, et al., "Room-Temperature Ferroelectricity in Hexagonally Layered α-In_2Se_3 Nanoflakes Down to the Monolayer Limit," *Advanced Functional Materials* 28, no. 50 (2018): 1803738, https://doi.org/10.1002/adfm.201803738.

47. C. Zheng, L. Yu, L. Zhu, et al., "Room Temperature In-Plane Ferroelectricity in van der Waals In_2Se_3," *Science Advances* 4, no. 7 (2018): eaar7720, https://doi.org/10.1126/sciadv.aar7720.

48. L. Wang, X. Zhou, M. Su, et al., "In-Plane Ferrielectric Order in van der Waals-In_2Se_3," *ACS Nano* 18, no. 1 (2024): 809–818, https://doi.org/10.1021/acsnano.3c09250.

49. L. Zhang and Q. Niu, "Chiral Phonons at High-Symmetry Points in Monolayer Hexagonal Lattices," *Physical Review Letters* 115, no. 11 (2015): 115502, https://doi.org/10.1103/PhysRevLett.115.115502.

50. M. Hamada, E. Minamitani, M. Hirayama, and S. Murakami, "Phonon Angular Momentum Induced by the Temperature Gradient," *Physical Review Letters* 121 (2018): 175301, https://doi.org/10.1103/PhysRevLett.121.175301.

51. H. Chen, W. Wu, K. Sun, S. A. Yang, and L. Zhang, "Electrically Controllable Chiral Phonons in Ferroelectric Materials," *Applied Physics Letters* 124, no. 9 (2024): 092201, https://doi.org/10.1063/5.0196731.

52. E. Oishi, Y. Fujii, and A. Koreeda, "Selective Observation of Enantiomeric Chiral Phonons in α-Quartz," *Physical Review B* 109 (2024): 104306, https://doi.org/10.1103/PhysRevB.109.104306.

53. Y. Long, S. Bu, H. Chen, et al., "Competing Ferroelectric Polarization and Defect Migration Induced Resistive Switching in β-In_2Se_3," *Nano Letters* 25, no. 7 (2025): 2922–2930, https://doi.org/10.1021/acs.nanolett.4c06314.

54. D. Zhang, D. Sando, P. Sharma, et al., "Superior Polarization Retention Through Engineered Domain Wall Pinning," *Nature Communications* 11, no. 1 (2020): 349, https://doi.org/10.1038/s41467-019-14250-7.

55. P. Miao, Y. Zhao, N. Luo, et al., "Ferroelectricity and Self-Polarization in Ultrathin Relaxor Ferroelectric Films," *Scientific Reports* 6, no. 1 (2016): 19965, https://doi.org/10.1038/srep19965.

56. S. Duan, M. Yang, S. Zhou, et al., "Efficient Terahertz Generation From van der Waals α-In_2Se_3," *Chinese Optics Letters* 22, no. 1 (2024): 013202, https://doi.org/10.3788/COL202422.013202.

57. J. Maysonnave, S. Huppert, F. Wang, et al., "Terahertz Generation by Dynamical Photon Drag Effect in Graphene Excited by Femtosecond Optical Pulses," *Nano Letters* 14, no. 10 (2014): 5797–5802, https://doi.org/10.1021/nl502684j.

58. P. Yordanov, T. Priessnitz, M.-J. Kim, et al., "Generation of Terahertz Radiation via the Transverse Thermoelectric Effect," *Advanced Materials* 35, no. 41 (2023): 2305622, https://doi.org/10.1002/adma.202305622.

59. Z. Lei, J. Chang, Q. Zhao, et al., "Ultrafast Photocurrent Hysteresis in Photoferroelectric α-In_2Se_3 Diagnosed by Terahertz Emission Spectroscopy," *Science Advances* 11, no. 7 (2025): eads8786, https://doi.org/10.1126/sciadv.ads8786.

60. N. Chudpooti, N. Duangrit, A. D. Burnett, et al., "Wideband Dielectric Properties of Silicon and Glass Substrates for Terahertz Integrated Circuits and Microsystems," *Materials Research Express* 8 (2021): 056201, https://doi.org/10.1088/2053-1591/abf684.

15214095, 0, Downloaded from https://advanced.onlinelibrary.wiley.com/doi/10.1002/adma.75389 by NICE, National Institute for Health and Care Excellence, Wiley Online Library on [23/10/2026]. See the Terms and Conditions (https://onlinelibrary.wiley.com/terms-and-conditions) on Wiley Online Library for rules of use; OA articles are governed by the applicable Creative Commons License

61. T. Seifert, S. Jaiswal, U. Martens, et al., "Efficient Metallic Spintronic Emitters of Ultrabroadband Tezrahertz Radiation," *Nature Photonics* 10 (2016): 483–488, https://doi.org/10.1038/nphoton.2016.91.

62. T. S. Seifert, D. Go, H. Hayashi, et al., "Time-Domain Observation of Ballistic Orbital-Angular-Momentum Currents With Giant Relaxation Length in Tungsten," *Nature Nanotechnology* 18 (2023): 1132–1138, https://doi.org/10.1038/s41565-023-01470-8.

63. G. Sala and P. Gambardella, "Giant Orbital Hall Effect and Orbital-to-Spin Conversion in 3d, 5d, and 4f Metallic Heterostructures," *Physical Review Research* 4 (2022): 033037, https://doi.org/10.1103/PhysRevResearch.4.033037.

64. T. Tanaka, H. Kontani, M. Naito, et al., "Intrinsic Spin Hall Effect and Orbital Hall Effect in 4d and 5d Transition Metals," *Physical Review B - Condensed Matter and Materials Physics* 77 (2008): 165117, https://doi.org/10.1103/PhysRevB.77.165117.

65. T. Funato, M. Matsuo, and T. Kato, "Chirality-Induced Phonon-Spin Conversion at an Interface," *Physical Review Letters* 132, no. 23 (2024): 236201, https://doi.org/10.1103/PhysRevLett.132.236201.

66. Y. Hirota, R. Hattori, M. Tani, and M. Hangyo, "Polarization Modulation of Terahertz Electromagnetic Radiation by Four-Contact Photoconductive Antenna," *Optics Express* 14, no. 10 (2006): 4486–4493, https://doi.org/10.1364/OE.14.004486.

67. Q. Yang, Y. Huang, H. Cheng, et al., "Broadband Polarization Spectrum Tuning Enabled by the Built-In Electric Field of Patterned Spintronic Terahertz Emitters," *Advanced Photonics* 7, no. 2 (2025): 026007, https://doi.org/10.1117/1.AP.7.2.026007.

68. N. Koirala, M. Brahlek, M. Salehi, et al., "Record Surface State Mobility and Quantum Hall Effect in Topological Insulator Thin Films via Interface Engineering," *Nano Letters* 15, no. 12 (2015): 8245–8249, https://doi.org/10.1021/acs.nanolett.5b03770.

Supporting Information

Additional supporting information can be found online in the Supporting Information section.

Supporting File: adma75389-sup-0001-SuppMat.pdf.

15214095, 0, Downloaded from https://advanced.onlinelibrary.wiley.com/doi/10.1002/adma.75389 by NICE, National Institute for Health and Care Excellence, Wiley Online Library on [23/10/2026]. See the Terms and Conditions (https://onlinelibrary.wiley.com/terms-and-conditions) on Wiley Online Library for rules of use; OA articles are governed by the applicable Creative Commons License